Lasers in Manufacturing Conference 2019

Simulation of solidification microstructures under thermal conditions of laser beam welding

Markus Apel[a,*], Oleg Stryzhyboroda[a], Guillaume Boussinot[a], Bernd Böttger[a]

[a]*ACCESS e.V., Intzestrasse 5, 52072 Aachen, Germany*

Abstract

Today, the phase-field method has reached a level of maturity that allows for spatially and temporally resolved simulations of the solidification microstructure evolution in technical, i. e. multicomponent and multiphase, alloys. In this paper, we will discuss two simulation examples: (i) laser welding of low-alloyed aluminum A3003 leading to cellular-dendritic microstructures, and (ii) welding of the nickel base superalloy IN718 showing more pronounced dendritic solidification structures. The simulations provide e. g. the cellular or dendrite spacing, the solidification path, i. e. solid fraction versus temperature, or the microsegregation pattern of the alloying elements. Based on these two examples we will remark on strategies to link local microstructure simulations with macroscale simulations of the thermal field and the accessible length and time scales for the microscale simulations. Furthermore, perspectives for applications in LPBF will be briefly addressed.

Keywords: solidification; microstructures; phase-field simulation;

1. Introduction

The re-solidified material in the weld seam undergoes various microstructural changes compared to the base material. In most cases, the microstructure is much finer because solidification in welding is much faster compared to the original processing of the base material, e. g. ingot casting. The modified microstructure alters the material properties in the weld seam accordingly. In addition, the tendency for defect formation, e. g. hot cracking, is intimately linked to the microstructure evolution during solidification, e. g. Beiranvand et al., 2019. Therefore, a physically sound understanding of the solidification kinetics and microstructure

* Corresponding author. Tel.: +49-241-8098009; fax: +49-241-38578.
E-mail address: m.apel@access-technology.de.

formation may help to assure the material integrity after welding, in particular for alloys prone to defect formation.

In recent years, phase-field models are technically mature to handle even complex technical multicomponent and multiphase alloys. This offers the opportunity to investigate the material response on laser beam welding considering the true chemical composition instead of using simplified material models, e. g. binary model alloys or approximations by linear phase diagrams. We will demonstrate this capability by comparing solidification microstructures of an A3003 Al alloy with those from an IN718 Ni base superalloy, assuming identical thermal gradients and cooling rates and confronting the simulation results with those from simplified analytical models. The focus of this article lies on a comparison of the primary dendrite arm spacing for both alloys.

2. Phase-field simulations

2.1. The multiphase-field model

We applied a general multicomponent multiphase-field model, see e. g. Eiken et al., 2006, linked to thermodynamic databases. The model is implemented in the software MICRESS, Micress website, 2019, which has been also used for the simulations. As thermodynamic databases, TCAL4 and TCNI7 from Thermo-Calc Software have been used, details about the database see Thermocalc website, 2019. For further reading about background and applications of the phase-field method, we refer again to the Micress website, 2019.

In the phase-field simulations the temperature field is described by the so-called “frozen temperature approximation”, i. e. the temperature field is superimposed on the simulation domain with no backward coupling from the microstructure evolution to the thermal field by the release of latent heat. This approximation is usually valid for processes with large temperature gradients when the internal heat sources are small compared to the external heat flux. The temperature gradient G in a laser welding process is typically in the range between 10^3 and 10^4 K/cm, and the liquidus temperature isotherm defined by the ratio $\dot{T}/G$ reaches velocities in the range of 1 to 10 cm/s.

The 2D computational domain size as represented in Fig. 1 and Fig. 3 is 25 µm $\times$ 44.4 µm. The number of grid points has been adapted to the microstructure length scales for the different cooling rates. The choice of identical domain sizes gives a straightforward visual impression how the characteristic length scales, e. g. tip radius or primary spacing, change with the cooling rate. A “moving domain” algorithm shifts the simulation box, keeping the distance d between the dendrite tips and the upper domain boundary constant (d = 10.5 µm). Periodic boundary conditions are applied along the horizontal axis. Additionally, long-range diffusion in the vertical direction is approximated by a 1D extension of the simulation box, which is attached to the upper boundary.

Material properties and further input parameters beside the thermodynamic properties taken from the databases as used in the simulation are listed in table 1.

2.2. Simulation Results for an Aluminum Alloy (A3003)

Low alloyed aluminum is used e. g. in the automotive industry for motor cooler components where laser welding is frequently part of the manufacturing process. The aluminum alloy composition considered in the simulations is Al-0.25Si-0.51Fe-1.17Mn [wt %] and comprises the major alloying elements of a commercial wrought A3003 alloy, but neglects trace elements or impurities. As the main topic of this paper is the selection of the primary spacing λ_1, only the primary fcc-phase is taken into account in the phase-field simulations. According to a Scheil-Gulliver computation, Al6Mn would be the second phase in the

solidification path emerging at about 50 % fraction solid, see also Fig. 5 (b), but should not play a role for the primary spacing selection.

Table 1. Additional material data applied for the phase-field simulations

An example of a column heading	Al-alloy		Ni-alloy	
Gibbs-Thomson coefficient Γ_{sl} [cm·K]	$2.27 \cdot 10^{-5}$		$3.00 \cdot 10^{-5}$	
anisotropy of interface stiffness[1] $\Delta\sigma^*$ [-]	0.288		0.288	
diffusion coefficients in the melt D_l [cm^2/s]	$1.3 \cdot 10^{-5}$	(Si)	$2 \cdot 10^{-5}$	all alloying elements
	$3.5 \cdot 10^{-5}$	(Fe)		
	$2.7 \cdot 10^{-5}$	(Mn)		
diffusion coefficients in fcc D_s [cm^2/s]	$9 \cdot 10^{-10}$	(Si)	T dependent, from mobility database MobNI4, between $0.7 \cdot 10^{-9}$ and $3 \cdot 10^{-9}$ for the different elements	
	$3.5 \cdot 10^{-9}$	(Fe)		
	$1.7 \cdot 10^{-8}$	(Mn)		

1) Interface stiffness $\sigma^* = \sigma - \sigma'' = 1 - \Delta\sigma^* \cdot \cos(4\Theta)$, σ is the surface energy and Θ denotes the angle between the surface normal and the crystallographic orientation.

The simulation example in Fig. 1 depicts the solidification morphologies simulated for three different cooling rates, $2.5 \cdot 10^3$ K/s, 10^4 K/s and $4 \cdot 10^3$ K/s, respectively. The temperature gradient $G = 10^4$ K/cm is constant for all three cases, and the cooling rate $\dot{T} = G \cdot v$ is proportional to the steady state solidification velocity. All three cases exhibit a dendrite-like morphology without side branches, and λ_1 decreases with increasing cooling rate.

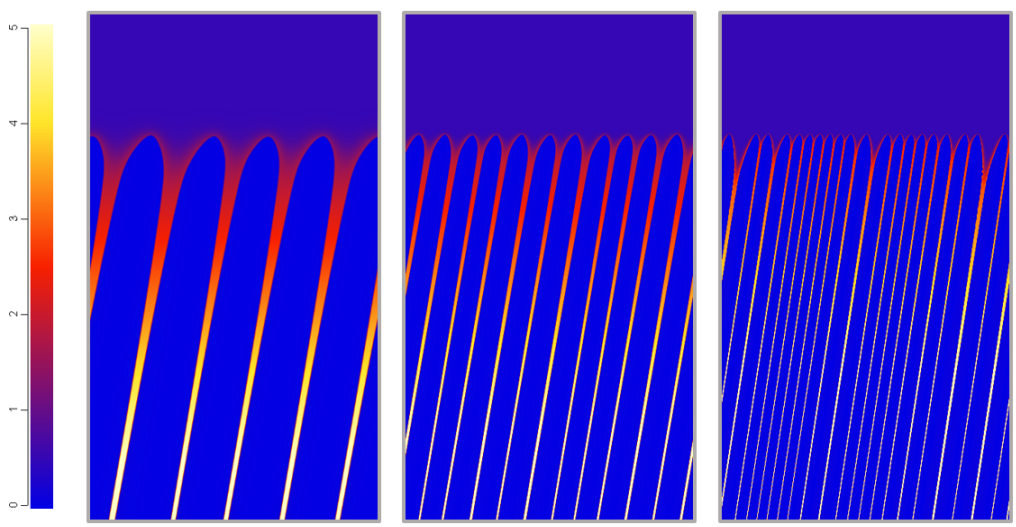

Fig. 1. Simulated solidification front morphology (represented by the Fe-concentration field) of A3003 for three different solidification velocities. Domain width is 25 µm. The thermal gradient points upwards, the preferential crystallographic growth direction ⟨100⟩ is tilted by 10°.

The absence of side branches can be explained by the fact that the tip radii r are not much smaller than the primary spacing, thus $r/\lambda_1 \rightarrow 1$ rather than $r/\lambda_1 \ll 1$, Boussinot et al., 2019. In other words, the liquid channel between neighboring dendrites is too small to allow side branching.

In Fig. 2 (a) a SEM image of the solidification structure in the weld seam of a laser welded A3003 sample is shown. The aligned microsegregation pattern also indicates a cellular/dendritic solidification structure without side branching with a primary spacing between 2 µm and 4 µm. This is consistent with phase-field simulations for $G = 10^4$ K/cm and velocities between 0.5 cm/s and 1 cm/s. Please note that λ_1 depends on G and v, thus one cannot derive both values independently from a single spacing measurement.

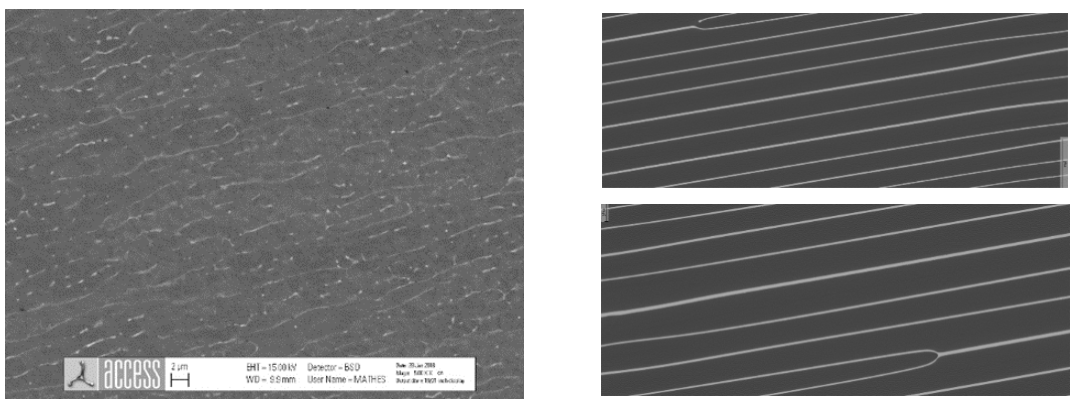

Fig. 2. (a) SEM image showing the solidification morphology of a laser welded A3003 alloy. The primary spacing is between 2 µm and 4 µm; (b) Grey scale representation of phase-field results for v = 1cm/s (upper image) and v = 0.5 cm/s (lower image), same length scale as the experimental picture in (a)

2.3. Simulation Results for IN718

The alloy IN718 and its derivatives are the most common Ni base superalloys for technical applications today. In direct comparison to the simulation for the aluminum alloy, Fig. 3 depicts the solidification morphology for Ni-17.6Fe-19Cr-5.13Nb-3.05Mo [wt %] which comprises the alloying elements with the highest fractions in IN718. Again, for the sake of simplicity, the formation of secondary phases is not considered in the simulation scenario, but could be included in a more comprehensive setting, Böttger et al., 2015.

The same values for the temperature gradient and cooling rate have been applied, thus Fig. 1 and Fig. 3 can be directly compared. The smaller tip radius for the Ni-alloy is directly visible, consequently side branches evolve, in particular for dendrites growing in a wider distance from its neighbor. Like in the case of A3003, simulations have been started from an initially almost planar front which exhibit initial perturbations of a wavelength smaller than the final spacing, so that the stationary spacing is a result of cell elimination processes.

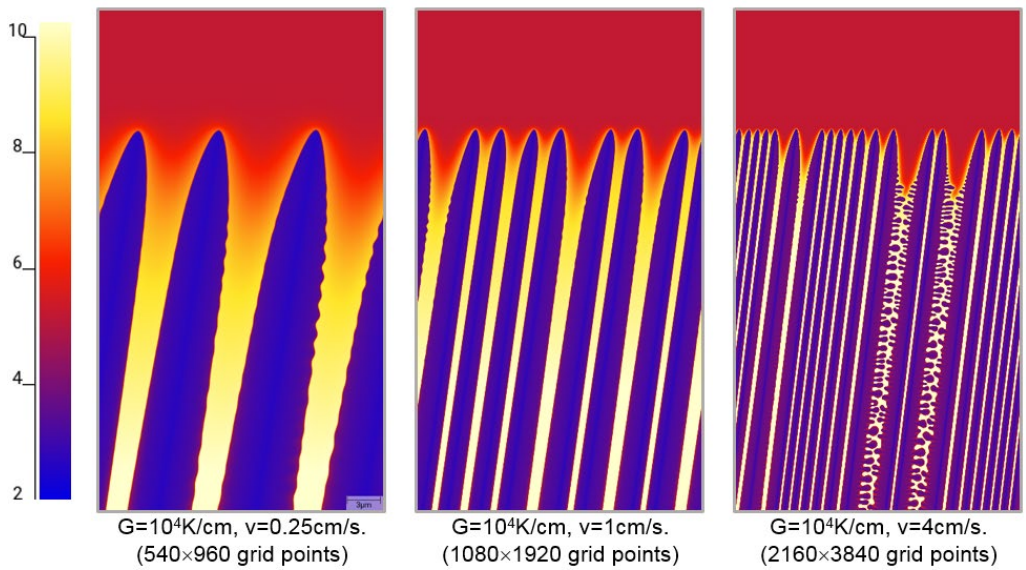

Fig. 3. Simulated solidification front morphology (represented by the Nb-concentration field) of IN718 for three different solidification velocities. Domain width is 25 µm. The thermal gradient points upwards, the preferential crystallographic growth direction ⟨100⟩ is tilted by 10°.

2.4. Simulations for the thermal conditions of LPBF

Laser powder bed fusion (LPBF) as an upcoming technique for additive manufacturing is widely used for 3D printing of IN718 parts already today. Because of the smaller melt volume and the limited preheating of the underlying material, thermal gradients and solidification velocities are larger for typical LPBF process conditions compared to laser welding. This will lead to an even finer primary spacing in the solidification morphologies. An example is shown In Fig. 4. For a larger temperature gradient $G = 5{\cdot}10^4$ K/cm and $v = 1$ cm/s an average primary spacing of $\lambda_1 = 0.87$ µm is found, compared to $\lambda_1 = 3.1$ µm for the same velocity but a smaller gradient $G = 5{\cdot}10^4$ K/cm as shown above. The microsegregation of all four alloying elements is represented in the figure. It can be seen that Nb is showing the largest concentration variations, and thus should be the mostly contributing element to the solutal pile up in front of the interface. The microsegregation also reflects the initial transient at the beginning of the solidification when starting from an almost planar front. In the first few microns no dendritic pattern has been established, followed by a somewhat finer structure at the edge of morphological instability. Similar features are frequently seen in the microstructure of LPBF printed materials as interlayer boundaries.

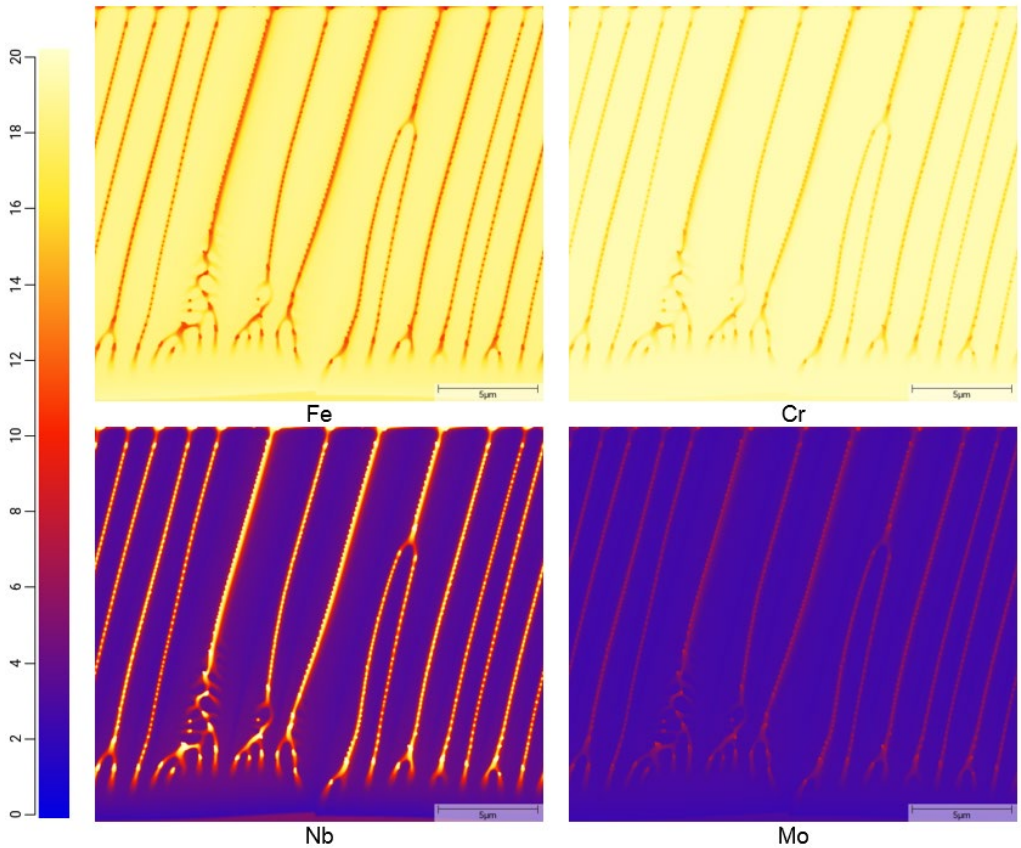

Fig. 4. Simulated microsegregation pattern for IN718 after complete solidification with v = 1cm/s and G = $5 \cdot 10^4$ K/cm. Identical color scale (in wt %) for all elements

3. Discussion

3.1. Primary spacing selection

From experiments as well as phase-field simulations it is known that the primary spacing λ_1 has no unique value. Instead, there is a finite range of spacings between λ_1^{min} and λ_1^{max} where a periodic dendritic array is stable against dendrite elimination or tertiary branching. The actual spacing of a dendritic array therefore is a result of the growth history. In our simulations we started from an almost flat front which develops perturbations at the onset of the morphological instability with a wavelength much shorter than λ_1^{min}. Therefore, we conclude that the present simulation setup leads to λ_1 values close to the minimal stable spacing λ_1^{min}.

The plot in Fig. 5 (a) shows the compiled data for a larger series of simulation runs. A simplified theoretical model for the primary spacing selection based on an elliptical envelope for the cells or dendrites and geometrical relations between the tip radius and the solidification length leads to the scaling $\lambda_1 \sim v^{-1/4}G^{-1/2}$, e. g. Kurz and Fisher, 1986. Therefore, the plot of the primary spacing over $v^{-1/4}$ should result in a linear dependency. However, the slope is sensitive on the tip shape, more precisely again on the ratio r/λ_1, or in

other words, the slope is different for solidification pattern build from shallow cells, deep cells or dendrites. We thus tentatively conclude that the change of slope from 3.3 µm/(cm/s)$^{1/4}$ to 7.4 µm/(cm/s)$^{1/4}$ seen in the spacing relation for A3003 below v = 1cm/s, is related to a transition between a "cellular-like" growth with interacting diffusion fields in the tip region to a "dendrite-like" growth regime with weakly interacting tips.

According to the analytical model $\lambda_1 = \alpha \cdot v^{-1/4} G^{-1/2}$, the prefactor α comprises all material related model quantities with

$$\alpha = \left(\frac{72\pi^2 \Gamma_{sl} D_l \Delta T_{sol}}{k_0} \right)^{1/4} \qquad (1)$$

See again Kurz and Fisher, 1986. It provides a further clue for the interpretation of the results from Fig. 5 (a). The material related quantities, i. e. the Gibbs-Thomson coefficient Γ_{sl} and the diffusion coefficients in the melt D_l, are rather similar for both alloys. The solidification interval shows a pronounced difference: according to the Scheil-Gulliver model around 77 K for the Al-alloy and 210 K for the Ni-alloy. This difference is somehow counterbalanced by the segregation coefficients k_0 which has a lowest value of 0.025 for Fe in Al and 0.453 for Nb in Ni (estimated from the local linear approximation of the phase diagram). Thus, for the same temperature gradient, the slope should not be too much different for both alloys, which is consistent with the phase-field results.

Nevertheless, estimating λ_1 by the analytical relationship has the limitation that this is valid only for a binary alloy. Inserting the small segregation coefficient for Fe in Al into the equation will lead to a primary spacing of about 18 µm for v = 1cm/s which is an order of magnitude above the phase-field result.

Increasing temperature gradients lead to a finer spacing. This is evident for the gradient variation at v = 1 cm/s for the Ni-alloy. Applying higher gradients also results in a smaller slope, which is the main reason why the LPBF solidification structures are finer compared to those obtained for laser welding conditions.

3.2. Comparison between phase-field and Scheil-Gulliver

The Scheil-Gulliver model (e. g. also in Kurz and Fisher, 1986) computes the solid fraction as a function of temperature under the assumption of no diffusion in the solid and perfect mixing (infinite diffusion) of the solute elements in the melt. This is a reasonable approximation of the solidification behavior and is often used to compute the solidification interval T_{sol}, but it neglects any dependency from the cooling rate. Thus, it has its limitations when describing transport effects for fast solidification. In Fig. 5 (b) predictions from the Scheil-Gulliver model, under the constraint that fcc is the only solid phase, are compared with phase-field results by plotting the solid fraction as a function of temperature, rescaled to the distance from the isotherm with equilibrium liquidus temperature T_m. The plot allows a direct comparison of the spatially resolved phase-field results with the thermodynamic Scheil-Gulliver computation. The dotted line for A3003 is the Scheil-Gulliver result taking into account secondary solid phases, which appear early in the solidification compared to the secondary phases in the Ni-base alloy (in this case more than 100 K below T_m). The curves obtained from the phase-field simulations show the growth undercooling of the front, ranging up to 12 K for the Al-alloy at v = 4 cm/s and up to 38 K for the Ni-alloy at the same solidification velocity.

Furthermore, the phase-field results cross the Scheil-Gulliver curves at a certain distance and then following the Scheil-Gulliver curve with an almost constant offset. The side branching in the solidification morphology for the Ni-alloy is reflected by the oscillations in the fraction solid curves at higher fractions.

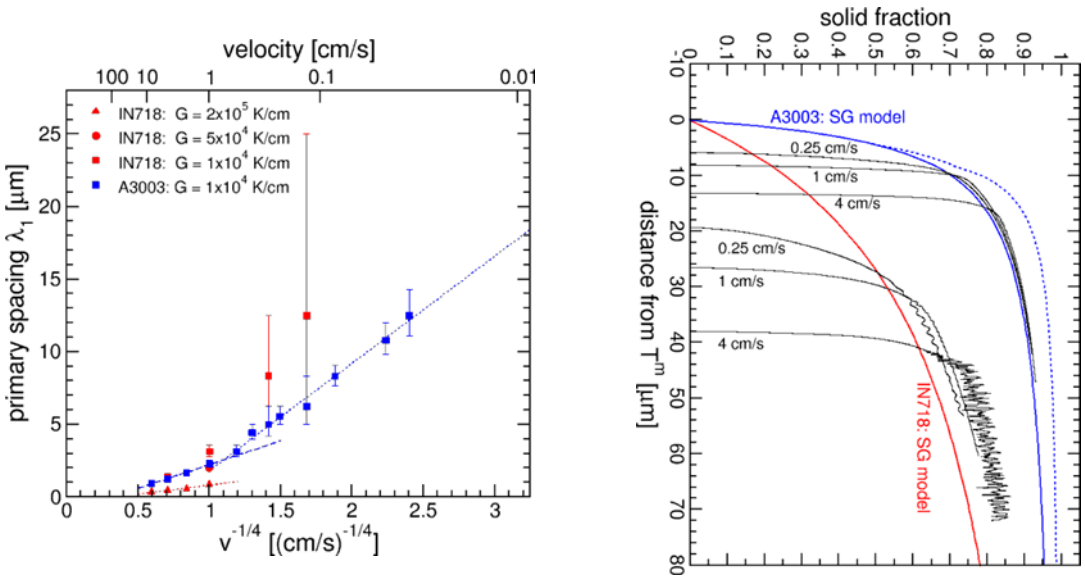

Fig. 5. (a) Primary spacing λ_1 dependent on the steady state growth velocity for both alloys. λ_1 is plotted over $v^{-1/4}$ respecting the analytical model for the primary spacing, see text. The error bars indicate the spread for ±1 dendrite in the simulation box; (b) solid fraction as a function of the distance from the liquidus temperature isotherm. Blue and red curves represent the Scheil-Gulliver model while the black lines represent the solid fractions from the phase-field results averaged over the horizontal direction. For G = 10^4 K/cm the distance in µm is equivalent to a temperature difference in K which has been applied to map the SG-data on a length scale

3.3. Scale bridging

As long as the frozen temperature approximation is valid, scale bridging to the thermal field defined on the scale of the melt pool is straightforward. Results from continuum scale simulations for the thermal field can be simply superimposed on the phase-field domain considering also the temporal changes of the cooling rate and/or thermal gradient.

Computational limitations for the feasible domain size for the microstructure simulations are set by the grid resolution required to resolve the smallest microstructural scale of interest, e. g. the dendrite tip radius r or the diffusion length l_d. As both quantities increase with smaller growth velocities it should be possible to increase grid spacing and thus domain size for lower cooling rates. However, another limitation is given by larger temperature gradients and the diffuse interface thickness of the phase-field model: the temperature differences over the diffuse interface should be sufficiently small in order not to interfere with physical quantities like curvature undercooling.

4. Summary and conclusion

Phase-field simulations elucidate the scaling behavior of the primary dendrite arm spacing λ_1 as a function of growth velocity for thermal conditions typical for laser welding and LPBF. The simulation results for multicomponent Al- and Ni-base alloys are consistent with simplified analytical models for binary alloys based on linear phase diagrams. The examples demonstrate the impact of the chemical composition on the spacing. For the same cooling rate and temperature gradient a low alloyed Al-alloy (A3003) exhibits a finer

solidification structure compared to a Ni-base alloy (IN718). Phase-field simulations allow a detailed and quantitative investigation of the solidification behavior along the solidification path which can provide crucial parameters for crack prediction models, e. g. Böttger et al., 2013 or Beiranvand et al., 2019.

Acknowledgements

We like to acknowledge financial support from the DFG in the framework of the collaborative research center “Precision Melt Engineering” (SFB1120).

References

Beiranvand, Z. M., Ghaini, F. M., Moosavy, H. N., Sheikhi, M., Torkamany, M. J., 2019. An Analytical Model for Prediction of Solidification Cracking Susceptibility in Aluminum Alloys Taking into Account the Effect of Solidification Rate, Metallurgical and Materials Transactions A, 50A, p. 2835.

Eiken, J., Böttger, B., Steinbach, I., 2006. Multiphase-Field approach for multicomponent alloys with extrapolation scheme for numerical application, Phys. Rev. E 73, 066122.

Micress website 2019. MICRostructure Evolution Simulation Software MICRESS, Version 6.4, www.micress.de.

Thermocalc website 2019. www.thermocalc.com.

Boussinot, G., Apel, M., Zielinski, J., Hecht, U., Schleifenbaum, J. H., 2019. Strongly Out-of-Equilibrium Columnar Solidification During Laser Powder-Bed Fusion in Additive Manufacturing, Physical Review Applied 11, 014025.

Böttger, B., Eiken, J., Apel, M., 2015. Multi-Ternary Extrapolation Scheme for Efficient Coupling of Thermodynamic Data to a Multi-Phase-Field Model, Computational Materials Science Vol. 108, p. 283.

Kurz, W., Fisher, D. J., 1986. Fundamentals of Solidification, Trans Tech Publications, ISBN 0-87848-522-3.

Böttger, B., Apel, M., Santillana, B., Eskin, D.G., 2013. Relationship between Solidification Microstructure and Hot Cracking Susceptibility for Continuous Casting of Low Carbon and High Strength Low Alloyed Steels: A Phase-Field Study, Metallurgical and Materials Transactions A, Vol. 44A (8), p. 3765.